Materials Today Communications 50 (2026) 114621

Contents lists available at ScienceDirect

Materials Today Communications

journal homepage: www.elsevier.com/locate/mtcomm

Biomechanical optimization of printing paths in Fused Filament Fabrication

Amelie Schiele [a,b], Iwiza Tesari [a], Christian Greiner [a,b,*]

[a] Institute for Applied Materials (IAM), Karlsruhe Institute of Technology (KIT), Kaiserstrasse 12, Karlsruhe 76131, Germany
[b] KIT IAM-ZM MicroTribology Center (μTC), Strasse am Forum 5, Karlsruhe 76131, Germany

ARTICLE INFO

Keywords:
Additive manufacturing
Fused Filament Fabrication
Biomimetic structural optimization
Computer aided internal optimization
Soft kill option

ABSTRACT

Additive Manufacturing has progressed from rapid prototyping to producing functional components. Extrusion based processes like Fused Filament Fabrication (FFF) enable fast, cost-effective fabrication of complex geometries, particularly in small quantities. However, the layer-by-layer structure leads to orthotropic mechanical properties, with strength and stiffness highest along print direction and decreasing in deviating directions. Designing robust components thus requires accounting for anisotropy and optimizing the printing paths themselves. Computer Aided Internal Optimization (CAIO), inspired by tree growth, aligns orthotropic axes with local principal stress, to match material strength and load paths. For a tensile-loaded perforated plate, the resulting orientation of orthotropic axes was translated into printing paths. Optimized specimens printed out of Polylactic Acid showed up to 28 % higher tensile strength, compared to industry-standard printing patterns using the same material amount. The Soft Kill Option (SKO), based on bone growth principles, was applied for topology optimization, targeting minimal mass and maximum stiffness. SKO optimized specimens achieved 25 % weight reduction and a 5 % increase in tensile strength over industry-standard prints. Compared to standard specimens of equal mass, breaking loads increased by nearly 70 %. These results demonstrate that CAIO and SKO significantly enhance mechanical performance and suggest strong potential for manufacturing highly robust components.

1. Introduction

Fused Filament Fabrication (FFF), also known as Fused Deposition Modeling (FDM), is a widely used 3D printing technique that offers much more design freedom for printable parts compared to classic manufacturing processes. This additive manufacturing process is based on a layer-by-layer deposition of material to create three-dimensional objects. FFF has gained popularity due to its low initial investment, wide range of applications, and ease of use [1]. The flexibility in printable geometry is one of the key advantages of FFF. The technology allows the creation of complex structures, including intricate internal geometries and customized designs. The ability to produce parts with varying infill patterns and densities further enhances the versatility of FFF in creating objects with specific mechanical properties [2]. Despite its geometric flexibility, FFF-produced parts often suffer from weak mechanical strength compared to traditionally manufactured components. This limitation is primarily attributed to the printing path orientation and layered structure [3], which results in local orthotropic material properties [4,5]. The greatest tensile strength is achieved when a uniaxial printed sample is loaded in the direction of the printing strands. In contrast, samples with printing strands oriented perpendicularly exhibit up to a 55 % reduction in tensile strength [6]. Furthermore, upright printed samples have the lowest shear strength [7]. This can be attributed to weak adhesion between the layers [8]. The stiffness and tensile strength are directly linked to the infill degree of the specimen, i.e. the ratio between strength and mass [2]. Typically, more material and denser infill patterns lead to increased strength [9]. The material properties in terms of tensile strength of FFF 3D printed Polylactic Acid (PLA) are orthotropic [6] with highest strength in the direction of the printing paths [7,10].

The optimization of 3D printing parameters is crucial for producing highly robust parts with minimal defects [11]. While many studies focus on interdependent parameters such as infill density, layer height, print speed, and extrusion temperature, these optimizations have limitations in addressing stress concentrations and notch effects inherent to component geometry. This necessitates the incorporation of structural optimization techniques to further enhance component strength. The potential for optimization lies in the stress-optimized infill layout of 3D

* Corresponding author at: Institute for Applied Materials (IAM), Karlsruhe Institute of Technology (KIT), Kaiserstrasse 12, Karlsruhe 76131, Germany.
E-mail address: christian.greiner@kit.edu (C. Greiner).

https://doi.org/10.1016/j.mtcomm.2026.114621
Received 30 October 2025; Received in revised form 12 December 2025; Accepted 2 January 2026
Available online 3 January 2026

printed components, whereby the structure of the components is adapted to the load during use [12]. Optimized printing paths and material distributions can reduce the amount of printed material and thus also the production time [13] and creating components with high load bearing capacity [2]. Other studies focused on optimizing printing paths based on principal stress direction, where print paths are planned according to load directions. The results showed significantly enhanced component properties in bending and tensile tests [14] [36]. Our study examines how biomechanical optimization(s) can increase tensile strength of FFF components and how printing paths can be derived from optimization simulation. It demonstrates approaches for an effective improvement of mechanical performance while simultaneously limiting the complexity and effort of the optimization. Biomechanical optimization in this work refers to an approach of biomimetics mimicking growth principals found in nature to enhance component properties [15]. Like FFF 3D printed materials and fiber-reinforced polymers, many naturally grown biological materials, such as wood, have orthotropic material properties [16]. Trees react to stress through adaptive growth and the orientation fibers in the direction of the force flow, according to their greatest load-bearing capacity [17]. Bone growth is also adaptive to stress. Bones accumulate more material in high stressed areas and remove it via demineralization processes in less stressed regions [18, 19]. Taking these mechanisms into account, and with use of the Finite Element Method (FEM), structural optimization of technical components according to biological growth principles is enabled. Soft Kill Option (SKO) and Computer Aided Internal Optimization (CAIO) create optimized structural designs based on Finite Element Analyses [20]. SKO simulates the mineralization and demineralization processes in bones and CAIO is inspired by fiber alignment in trees [17]. It was originally developed to locally align the fiber orientation along the principal stresses in fiber-reinforced composites [21]. The orientation of the fibers along the force flow increases the load-bearing capacity and stiffness of the composites significantly [22]. CAIO is used in this work to adapt the printing path orientation to the stress and to increase the tensile strength of the printed structure. As an example, the stress distribution in a tensile loaded plate with a hole is investigated. First, the orientation of the main stress trajectories are determined using the finite element method and subsequently CAIO optimization is applied in order to determine the printing paths for FFF additive manufacturing. In addition to the flexibility of FFF in terms of printable geometries, the lightweight potential is a key advantage of the manufacturing process. In order to create a lightweight yet strong component, the perforated tensile specimen is adapted using SKO. SKO is a topology optimization method, in which areas with high load are maintained and lower loaded areas are only filled with a low infill density.

2. Experimental

To evaluate the tensile performance of the optimized specimen types relative to industry-standard prints, sets of CAIO optimized specimens and a set of SKO optimized specimens were manufactured and subjected to tensile testing. For comparison, reference specimens featuring various standard printing patterns were likewise fabricated and tested. For each specimen type, five samples were produced and tensile tested.

2.1. Sample geometry

The influence of structural optimization of printing patterns in FFF 3D printed components under tensile load was investigated, using the example of a flat, perforated tensile specimen based on DIN EN ISO 527 [23], shown in Fig. 1. The perforated plate is a simple and representative geometry, which is common in actual component layout. It therefore is a highly practical example to test the applicability of both optimization methods. The height of the specimen was chosen as 3 mm and the hole diameter at 5 mm. The width was set to 15 mm and the length of the testing zone to 50 mm and with 140 mm being the total length of the specimens.

2.2. Computer Aided Internal Optimization

A two dimensional geometry model of the perforated plate was created in ANSYS MAPDL (Ansys, USA). Initially, the orthotropy axis were oriented in the direction of the global coordinate system. Due to the different stiffness of additively manufactured samples parallel and perpendicular to the printing path [8], an anisotropy in stiffness of 10 % was assumed in the model, set as effective Young's modulus. Parameters are listed in Table 1.

Because of symmetry of the perforated plate, a quarter was modelled and later the entire sample put together by mirroring the results. After generating the model's geometry, a mesh with four-node elements was created. Areas experiencing high loads and stress gradients were meshed more densely. After setting boundary conditions and applying a tensile load, the stress state was calculated. Boundary conditions define clamping of the geometry. For the FEM analysis a plane stress and strain state were assumed. This assumption is warranted as the perforated plate has a uniform thickness, which is less than the crosssectionional dimension and the plate is in-plane loaded [24]. CAIO was implemented in with ANSYS MAPDL (Ansys, USA). After a classical FE analysis, CAIO determines the angle between the global coordinate system and the

Table 1
Parameters of the FEM simulation.

Parameter	Value
Effective Young's modulus x direction	10 000 MPa
Effective Young's modulus y direction	1 000 MPa
Poisson's ration	0.3
Element type	PLANE 182
Area load	-1 N

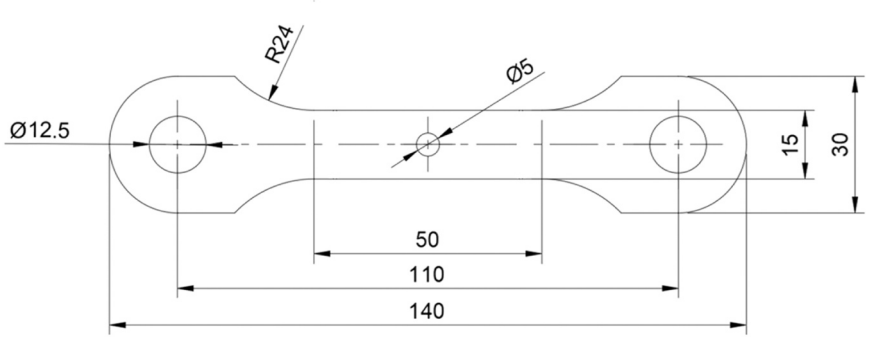

Fig. 1. Shape of perforated tensile specimen based on DIN EN ISO 527 with clamping and testing zones. This is a highly representative geometry as it is commonly used in component design.

principal stress direction in each element. The method then rotates the orthotropic axis with the greatest stiffness in the direction of the force flow, i.e. in the direction of the 1st principal stress. As the local orthotropy axis is rotated, the material properties change and so does the force flow. With the change of material properties, a new FE analysis has to be performed to determine the new stress state. The CAIO calculation and the FE analysis were iterated two times until no significant change in the rotation angle could be determined [14].

2.3. Soft Kill Option

The SKO method (Soft Kill Option) is a topology optimization method for lightweight construction applications. It aims to optimize components for maximum stiffness and strength, while minimizing material usage [17]. The method variates the stiffness in a structure, increasing the stiffness of elements that carry more load and decreasing the stiffness in elements that carry less load [25]. In this context, stiffness is represented in the model through a spatially variable Young's modulus. However, this parameter does not correspond to the actual material property in a physical sense. To emphasize this distinction, the model parameter is referred to as the effective Young's modulus. The SKO optimization approach is based on the natural inspiration found in bone growth. There, mineralisation or demineralisation is controlled by mechanical load [18]. As mechanical stresses increase, bone material is deposited in greater quantities, locally making the bone stiffer. In contrast, areas subjected to lower loads undergo bone resorption, leading to a reduction in bone mass [18,26].

The SKO method starts with a FEM analysis to determine the stress distribution for the anticipated loading scenario of the component. It is essential that the model geometry includes the optimized shape entirety. Boundary conditions are set to define the clamping of the geometry. First, a constant stiffness, set as effective Young's modulus, is assumed over the entire geometry in the simulation. The effective Young's modulus is then varied depending on the locally occurring stress. The stress distribution is recalculated for the same load, but with a spatially varied effective Young's modulus [25]. The variation of the effective Young's modulus is incremental and defined as a function of temperature for each element. The temperature is chosen as the control variable because it makes SKO easy to adapt to any FEM programme, as these all contain temperature-dependent Young's modulus parameter. Areas with a maximum set temperature are assigned the maximum effective Young's modulus, while below a certain temperature the minimum effective Young's modulus is assigned, with a linear relationship in between [27]. With each iteration, a new temperature is assigned to each element based on the difference between the calculated and the reference stress and an adjustment parameter b. The parameter b, between 0 and 1, magnifies the influence of the difference between the calculated and the reference stress. Here b was set as 1.

$$E_{n+1} = \quad E_n + b(\sigma_n - \quad \sigma_{ref})$$

The method allows the use of different stresses. Here, the von Mises equivalent stress was used. A specified reference stress σ_{ref} serves as target value. It is a predefined value that is valid for the entire volume. The optimization is most effective if the reference stress is initially set to a small value and then gradually increased. The higher the reference stress is set, the more material is removed [25]. Elements that reach or exceed this reference stress should finally have the maximum elastic modulus. Elements that are loaded below the reference stress are softened. The effective Young's modulus moves linearly within a range between E_{max}= 1000 MPa and E_{min}= 1/1000 E_{max}, i.e. no element can become stiffer than the material. And even when completely unloaded, it cannot become softer than 1/1000 of this value and is not removed during the iterations [17].For each reference stress of 5 MPa, 7 MPa, 10 MPa and 11 MPa, ten iterations were performed. This procedure enables a clear distinction between regions characterized by high and low stiffness. Based on the area with stiff elements, a CAD model was created and the sample manufactured.

2.4. Translating the CAIO optimization into G code

To transfer the CAIO optimization results into a printable part, G Code has to be generated after the simulation. In order to do so, the printing paths are set to follow the principal stress trajectories found by the CAIO method. When the printing paths are orientated along the principal stress direction, they are automatically also oriented along the force flow and thus in the direction of their greatest load capacity [21]. The coordinates along the principal stress trajectories were read in ANSYS MAPDL (Ansys, USA) by a self-written script. The script uses the rotation angles of orthotropic axis, resulting from the optimization, to follow the trajectories and extract the path coordinates. The modelling was again performed on a quarter model; the coordinates were mirrored in order to generate a path over the entire length of the sample. CAIO uses the Euler angles of the principal normal stress (PNST) calculated to orient the material coordinate system of each element along the first PNST. The principal stress directions of each element are estimated in ANSYS APDL with the *VFUN command which calculates the Euler angles of the principal stresses. With this, CAIO aligns each element materials coordinate system to the principal stress direction at the elements centre. This ensures that the direction of highest material stiffness in the simulation corresponds locally to the direction of highest stress. This is a plane problem, which means that it is sufficient to consider the Sx, Sy and Sxy stress components. The printing paths are created based on the simulation results. First, for each printing path a starting point is selected. The starting points of the path coordinates were located at the narrowest point of the model, where the stress concentration caused by the hole is greatest. The starting points were placed with the distance of one strand width. At each starting point, the stress state is queried and the direction vector of the first PNST is generated using the Euler angles. Starting from there, the next point is generated using the direction vector and a specified distance, and the extrusion amount is calculated. This process is repeated until the printing path reaches the edge of the part, where it ends. The coordinates of the paths were subsequently extracted and exported as a text file. The text file was converted to G Code by a self-written python script.

The G Code is based on several standard commands, each beginning with the letter G or M. The G0 and G1 commands correspond to a linear movement between printhead and platform to a defined location with a given speed. G0 is a command for fast machine movements without extruding material. The G1 command uses in addition to the coordinates of the extruder movement a fourth dimension E. The E value defines the cumulative amount of the filament that is fed through the nozzle [28]. A typical command has the following form:

```
G1 X10 Y20 Z0.2 E5 F1200
```

In this example, the printhead moves to the position x = 10 mm and y = 20 mm, at a height of z = 0.2 mm, with a speed of 1200 mm/s and extrudes filament. The extrusion quantity is determined by multiplying the cross-section of the extruded material by the length of the section to be extruded [29]. In the area where the sample geometry widens behind the hole, the paths are separated by gaps. If the gaps are of sufficient size, a new path was inserted. Low stressed areas were not optimized and were filled with a standardized, crossed line pattern with a grid angle of + /- 45°, generated by the slicing software UltiMaker Cura (UltiMaker, Netherlands).

Since this optimization is limited to the printing plane, the printing commands were repeated in each layer, up to the specimen high of 3 mm. While the middle part of the specimen was printed according to the optimization results, the clamping zone was filled with a standard cross line pattern, generated by the slicing software UltiMaker Cura.

2.5. G Code for SKO optimized structures and reference specimens

The result of the SKO optimization is a component that primarily consists of structural elements subjected to tensile stresses, as less loaded areas have been removed. In order to translate the SKO optimization to the printed component, the tested area of the specimen was divided into two zones in the slicing software. The zones were selected by placing a support block over the designated volume resulting from SKO. This approach enabled the assignment of independent printing parameters to each zone, distinct from those applied to the remaining volume: the stiffness in areas with low effective Young's modulus from the SKO optimization was reduced by decreasing the filling density down to 20 %, while areas with high effective Young's modulus were set to 100 % infill density. In areas with 100 % filling density, a line pattern was selected in the tensile direction and a grid pattern in the less densely filled areas.

The workflow for standard and optimized specimens differed in creating the model and further generating the machine code for the 3D printer. The manufacturing process of the reference specimens started with modelling the part geometry and creating a 3D volume model in the CAD software Autodesk Fusion 360 version 2.0 (Autodesk, USA). The link between volume model and the printer is the slicing software that generates the G Code [30]. Printing parameters such as layer thickness and temperatures were defined there and are listed in Table 2.

There are a large number of different pre-set standard patterns in most slicers that could be used to fill printed parts. Common structures are lines or grid patterns, which were variated in size and infill density [31]. Four types of specimens were designed for reference experiments, illustrated in Fig. 2:

1. Layer-by-layer alternating + /- 45° line pattern, with 100 % infill density.
2. Longitudinal line pattern, also at 100 % infill density.
3. Alternating longitudinal and transverse (0°/90°) strands, 100 % infill density.
4. Longitudinal line pattern, but with a reduced infill density of 75 %.

The G code for the reference specimens was generated with the slicing software UltiMaker Cura.

2.6. Printing

Polylactide Acid (PLA) is a very commonly used FFF filament material, due to its good availability, low cost, non-toxicity, flexibility and fast printability [1]. It was therefore used for the samples tested here. All specimens were printed with a standard Creality Ender 5 S1 printer (Creality, China) and the same filament batch and general setup. In order to compare and quantify the load bearing capacity of all specimens, five samples of each type were printed. A filament wire is melted by a hotend in the printhead and applied to a heated printing bed via a nozzle [32]. The filament is pushed through the nozzle by a direct extruder. The overall geometry is created layer by layer, with each layer formed of a pattern of individual printing strands [33].

Table 2
Printing parameters of the slicer generated G code.

Parameter	Value
Nozzle diameter	0.4 mm
Nozzle temperature	205 °C
Built plate temperature	60 °C
Layer thickness	0.2 mm
Strand width	0.42 mm
Printing speed	120 mm/s
Filament material type	ecoPLA light gray (3DJAKE, Austria)

2.7. Sample characterization and tensile testing

The weight of each sample was measured with a precision scale and accuracy to one milligram. In order to investigate the effect of the optimized filling patterns, five samples of every specimen type were subjected to a tensile test using an Instron 1185 universal testing machine (Instron GmbH, USA).

The tensile testing machine consists of a stationary and a movable crosshead, which was moved at a constant speed of 2 mm/min. During the tests, the deformation of the specimens over the movement of the crosshead was measured with an inductive displacement transducer and the applied force was measured with a 10 kN load cell which has an accuracy of ±0.5 % (Reading Down, England). Data acquisition was performed using DasyLab 7.0 (National Instruments, USA).

3. Results

3.1. FEM results for the CAIO method

The FEM analysis determined the principal stress distribution. The notch effect of the perforation creates a stress concentration at the rim of the hole. The stress distribution and the material properties are changed by the rotation of orthotropic axis in the elements, displayed in Fig. 3. After the first CAIO calculation, a new FEM analysis was carried out to determine the new stress state. The stress concentration at the edge of the perforation increased after the CAIO calculation, which seems contradictory. However, since a low stiffness in the direction of the tensile load was initially defined in the model, the stress concentration at the edge of the hole is lower, and so is the strength. Due to the rotation of the orthotropic axis, the stress concentration at the notch increased. With the orientation of the printing paths along the principal stress direction, the tensile strength of the printed specimen is expected to increase. The CAIO method converged quickly, meaning that in subsequent iterations the course of the principal stress trajectories, as well as the stress state, hardly changed [20]. Here, for the perforated plate the CAIO analysis was iterated two times, demonstrating the efficiency of the method.

The result of the CAIO method is the orientation of the orthotropic axis and the principal stress in every element in the model. By extracting the coordinates of the principal stress trajectories, paths are extracted, as shown in Fig. 4. A Python script filled the gaps between the paths. The rim of the specimen was filled with vertical paths and the low stressed area(s) were filled with a + /-45° altering line patterns.

3.2. SKO results of and transfer to infill patterns

The SKO optimization aims at the reduction of material/weight by adjusting the infill quantity and the print pattern. The same FEM geometry model as in the CAIO optimization was used and mirrored, to get a full model. After defining boundary conditions and the load, the stress field was calculated and the SKO calculation started. In Fig. 5 the distribution of the effective Young's modulus calculated with differently set reference stresses is shown. Elements reaching the upper limit of the effective Young's modulus are coloured red, while those reaching the lower limit are coloured blue.

The SKO results obtained for stress reference values of $\sigma_{ref} = 5$ MPa and $\sigma_{ref} = 7$ MPa revealed a localized reduction in the effective Young's modulus confined to a small region above the perforation, shown in Figure 1Fig. 5 indicated in blue. Due to the limited extent of this low stiffness area, the potential for material reduction was minimal. Consequently, these configurations were excluded from further consideration for the design of the printed specimen. In contrast, the SKO simulation with $\sigma_{ref} = 11$ MPa produced a more extensive low stiffness region both above and around the perforation, along with a narrow low stiffness area at the specimen's edge, shown in Figure 5. Transferring this result into a printable design would necessitate an adjustment of infill density along the thin rim. Since the rim's width approximately

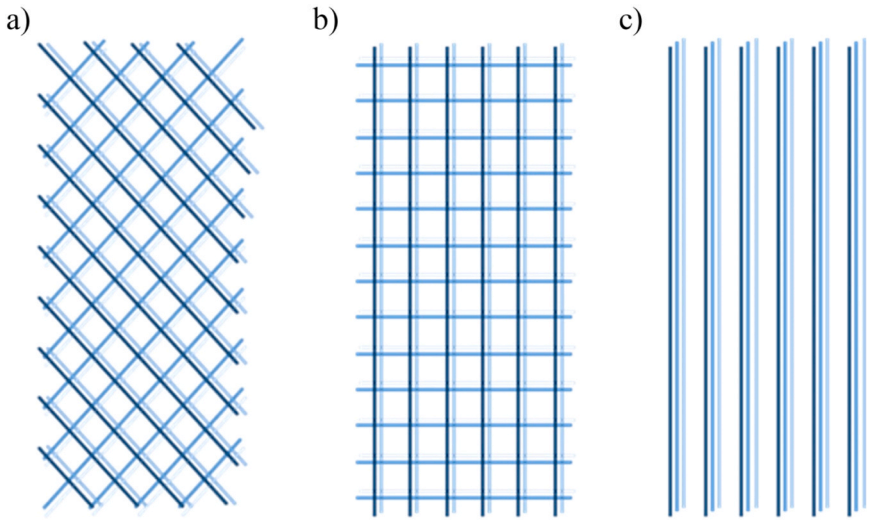

Fig. 2. Three standard patterns used for reference specimens. a) layer-by-layer alternating + /- 45° line pattern, b) alternating longitudinal and transverse (0°/90°) strands, c) longitudinal line pattern.

matches the size of a single printing strand, any contour required to enclose the structure would overlap with the optimized region, thereby obscuring the optimization result. With that the feature would not be printable. The SKO outcome at $\sigma_{ref} = 10$ MPa, in contrast, displayed a broad low stiffness region without any excessively fine, unprintable features. Thus, this configuration was selected for implementation in the printed specimen. Fig. 6 illustrates the resulting infill layout derived from the SKO optimization. To translate the SKO result into G code, the identified regions were assigned distinct infill densities and patterns tailored to the local effective Youngs' modulus. Because of the regular shapes of the resulting regions, they were assumed as blocks. This approach enabled a total material reduction of 25 % compared to a 100 % filled structure.

3.3. Printing results

Fig. 7 shows three different reference samples, next to a CAIO optimized sample (Fig. 7a). The three standard filled specimens, filled with 100 % infill density are used for comparison to the CAIO optimization, are with a layer-by-layer alternating + /- 45° line pattern (Fig. 7b), with a longitudinal line pattern (Fig. 7c) and with alternating longitudinal and transverse (0°/90°) strands (Fig. 7d). A set of five samples were printed for every variant.

Fig. 8 shows the printing results of reference samples, next to a SKO optimized sample (Fig. 8a). In this case, completely filled (Fig. 8b) and 75 % filled (Fig. 8c) specimens were chosen as a reference. In the 75 % filled specimens, the amount of material used corresponds to the SKO optimized specimens. The reference specimens are filled with a standard line pattern in the direction of the tensile load. Here, as well a set of five samples were printed for every variant. The 100 % filled samples correspond to the reference also chosen for the CAIO comparison.

3.4. Tensile test results for CAIO optimized samples

In order to compare the amount of printed material across the specimens, all samples were weighted. In addition, the theoretical extruded material was calculated using the quantity of extruded material, defined in the G Code. With a wire thickness of 1.75 mm, the mass was calculated using the cross-sectional area of the wire, the wire length and the density of PLA (1.2 g/cm^3). Table 2 presents the calculated mass for all specimen types, the measured mass, and the corresponding standard deviations. Five samples of all four specimen types were measured. The theoretical and average total mass of the samples matched with a difference of less than 0.5 %.

On all five samples of every specimen type a tensile test was conducted. Representative example of post-mortem samples are presented in Fig. 9. All samples, independent of being optimized or not, failed next to the hole. All CAIO optimized samples shoes chipping (Fig. 9a). Fig. 9b presents the average breaking load for each specimen type. The CAIO optimized samples achieved an average breaking load of 1681 N and a standard deviation of 39 N. Specimens with 0° line pattern failed at an average breaking load of 1530 N and standard deviation of 6 N, while the samples of specimens with altering line pattern of + /- 45° and 0°/90° had breaking loads of 1351 N and 1312 N with standard deviation of 43 N and 13 N. The CAIO optimization thereby increased the breaking load by 10–28 %, compared to conventionally generated FFF prints with the same amount of material.

3.5. Tensile test results of SKO optimized samples

Representative post-mortem samples are presented in Fig. 10a, while in Fig. 10b the average breaking loads are plotted for the SKO optimized specimens and compared to the two references types detailed above. On all five samples of every specimen type a tensile test was conducted. These tensile tests revealed that the SKO optimized samples did not fail at the hole, in contrast to all other samples. The SKO optimized samples fail close to the transition of testing to clamping zone. For the reference specimens, an increase in breaking load is observed with increasing filling density: From an average of 952 N and standard deviation of 13 N at 75 % infill density to 1530 N and standard deviation of 6 N at 100 % infill density, which equals an increase by a factor of 1.6. The optimized specimens had an average breaking load of 1613 N with standard deviation of 21 N. With the same amount of material, meaning a 75 % infill density, the average breaking load of the optimized specimen was almost 70 % higher than for the reference samples. The SKO optimized specimens showed a 5 % higher average breaking load compared to the 100 % filled reference specimens, despite a 25 % reduction in used material.

4. Discussion

Based on the assumption that the printing path orientation in FFF 3D printed components has a similar influence on the load-bearing capacity as the fiber orientation in fiber-reinforced materials [21], printing paths and so the structural properties of the infill in terms of tensile strength were optimized with CAIO. The inner structure was adapted to the

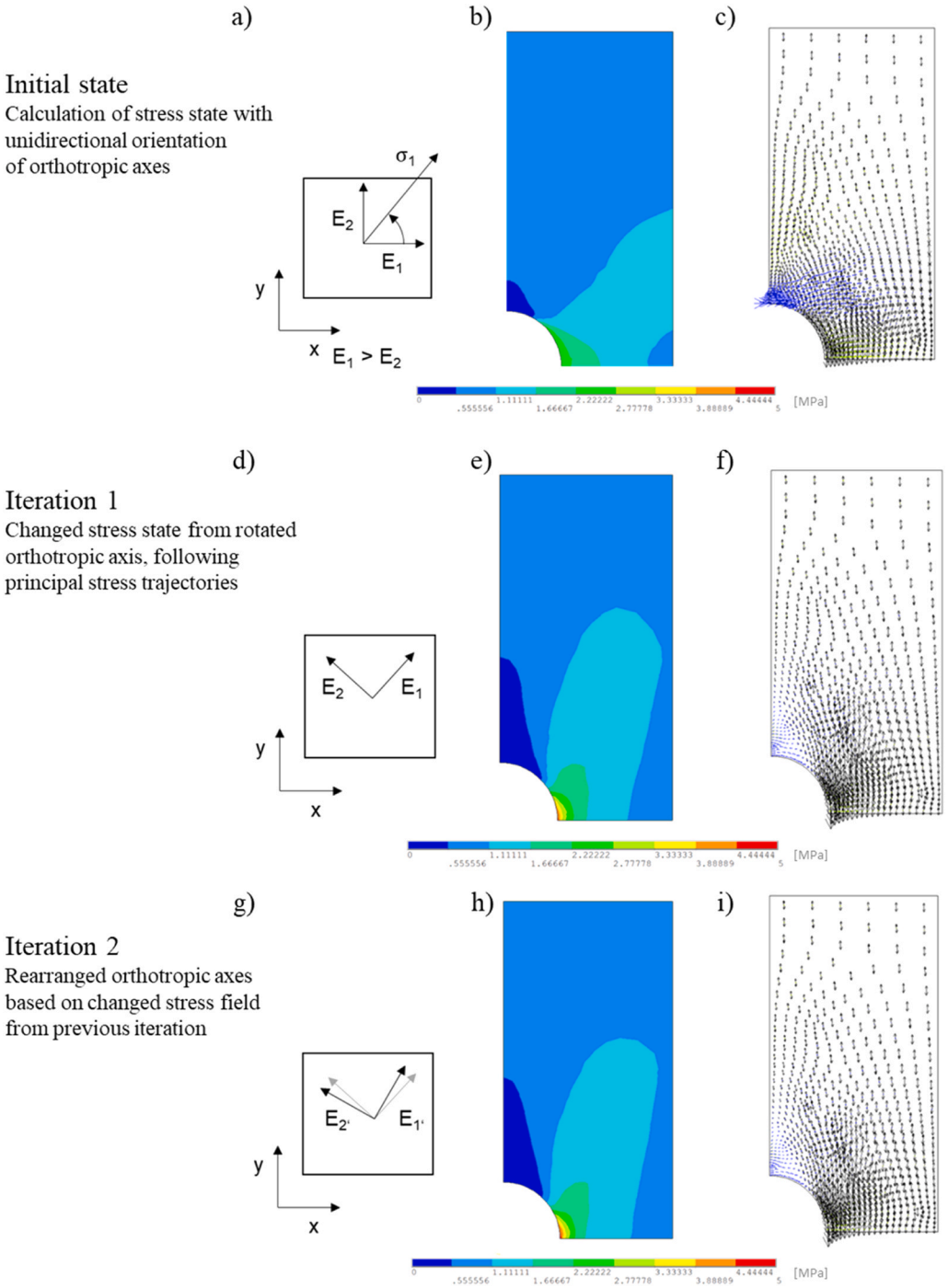

Fig. 3. Iterations of CAIO method as it rotates the orthotropic axis of every element. This changes the material properties and thus the stress distribution of the next iteration. In the initial state all elements have their orthotropic axes in the direction of the coordinate system (a), creating a highly stressed area next to the hole through a notch effect (b). The principal stress vectors are shown for each element (c). After the first CAIO iteration, the orthotropic axes are rotated in the direction of the principal stress (d). As the stress field changes (e), the orientation of the principal stress is also changing (f). In the second iteration the stress is calculated for a third time (h) with the new orthotropic properties (g). The directions of the principal stress vectoes are resulting from second CAIO iteration (i).

stresses in the component, by orienting the printing paths in the direction of the principal stress trajectories. In the past, numerous studies have demonstrated the benefits of printing path optimization [33–36]. In practice, however, there are inevitably deviations between the modelled and the manufactured component, which affect the effeciveness of the optimization. This is particularly relevant when optimizing the local printing path orientation, by aligning the path direction with the principal stress orientation. In FE simulations using ANSYS MAPDL, the principal stress vectors are available at every mesh location, providing a vector field across the model. From this field, streamlines can be computed to represent the printing paths that follow the principal stress direction [37]. The distance between two neighbouring streamlines can change considerably in the model, but the overlap or the width of a printed strand can only change to a small extent. For PLA, strand width can vary around ±20 % of the nominal value without major loss in mechanical performance [38]. This can easily lead to gaps or excess material between the printed strands, resulting in additional sources of stress concentration. These practical limitations must be considered

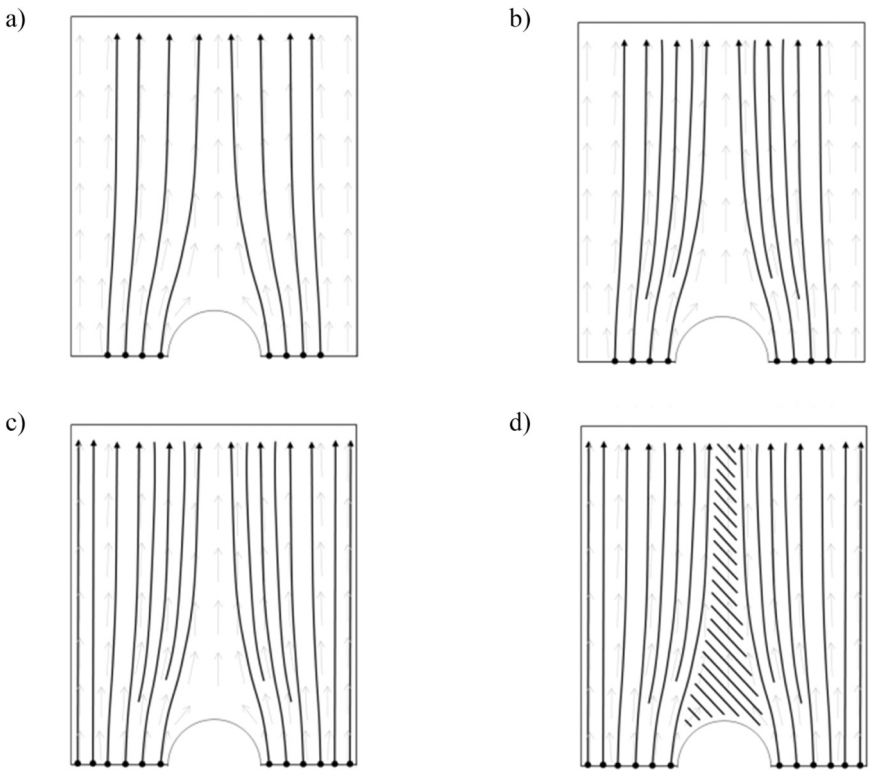

Fig. 4. Generating printing paths based on the CAIO results: a) generation of the printing paths along the principal stress trajectories, starting from the narrowest point of the model, where the stress concentration caused by the hole is greatest; b) filling of gaps between the paths; c) principal stress direction in the edge area barely deviates from the vertical direction; d) weakly stressed areas filled with standard filling pattern + /-45°.

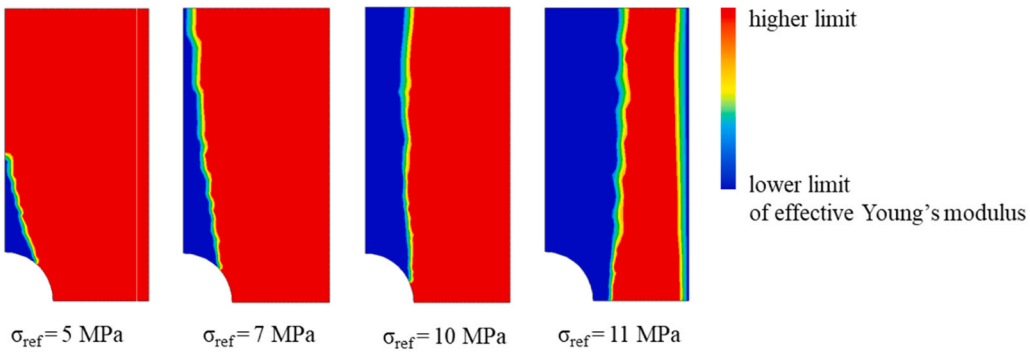

Fig. 5. The variation of the effective Young's modulus (red: high, blue: low) depends on the chosen reference stress (σ_{ref}). The higher the reference stress is set, the more elements reach the lower limit of the effective Young's modulus.

when translating optimized printing paths orientations into real-world printing strands. To address this, the present work focuses the CAIO optimization method specifically on the highly stressed regions of the component. By placing the printing paths in an ideal distance at the highest stressed regions, the risk of gaps or over extrusions in the region critical to failure is minimized. In contrast, the low stress regions are filled using conventional line patterns, significantly reducing computational effort. The optimization potential and practical feasibility were verified experimentally. The CAIO optimized specimens exhibited a higher braking load than the reference specimens. Compared to the specimen with altering line pattern of 0° and 90°, an increase in breaking load of up to 28 % was achieved. Compared to the longitudinal printing paths, which is a form of pre-optimization as the printing direction aligns with the load direction, the CAIO optimized specimen show an increase in breaking load of 10 %, even though the orientation of the printing path is mostly similar in both specimens, apart from the areas close to the perforation. The discrepancies in weight of all specimens without the reinforcement layers, calculated from the theoretical mass, is 0.5 % and can be neglected. The difference in the total weight of the optimized and reference specimens is attributed to the reinforcement layers in the clamping areas for some specimens. Consequently, the improvement in tensile strength is realized by adjusting the printing path orientation in particularly stressed areas with constant material usage.

With the SKO optimization, the mass could be reduced by 25 %, while at the same time the specimens showed an increase in breaking load of about 5 % compared to the standard filled ones with 100 % infill density. An even more significant increase in breaking load of almost 70 % was realized compared to specimens of the same mass. While fiber-reinforced filaments are commonly used to improve strength-to-weight ratio [39], this work shows that SKO can significantly enhance the mechanical properties of 3D printed parts, even with standard PLA and

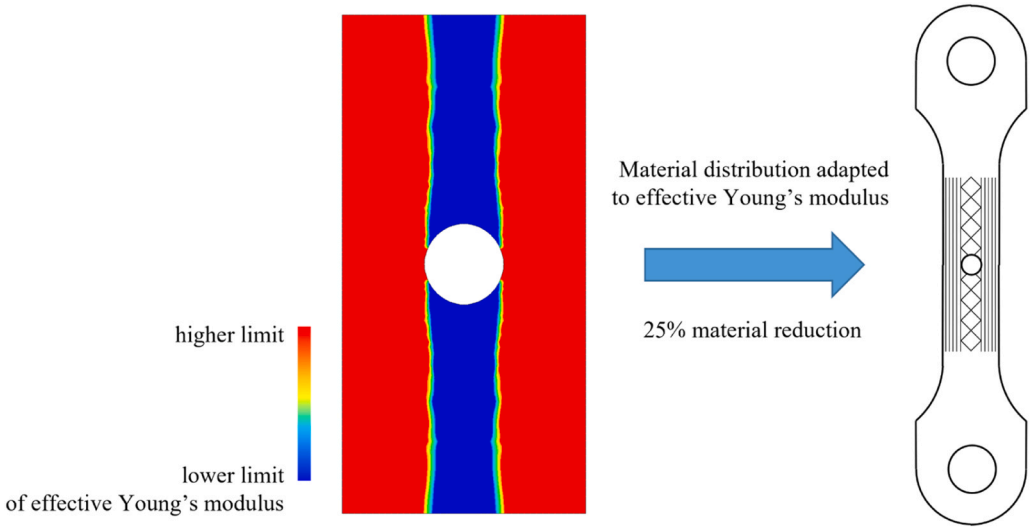

Fig. 6. SKO results with $\sigma_{ref} = 10$ MPa (left), which divides the model in areas of high (red) and low (blue) effective Young's moduli. In order to transfer the optimization result into printing paths, the areas are filled with two levels of infill density and the suitable pattern (right). The red areas is filled with 100 % infill density and line pattern, as they are under a tensile load. The blue area is filled with a grid pattern, as a standard pattern for internal structures with an infill density of 20 %.

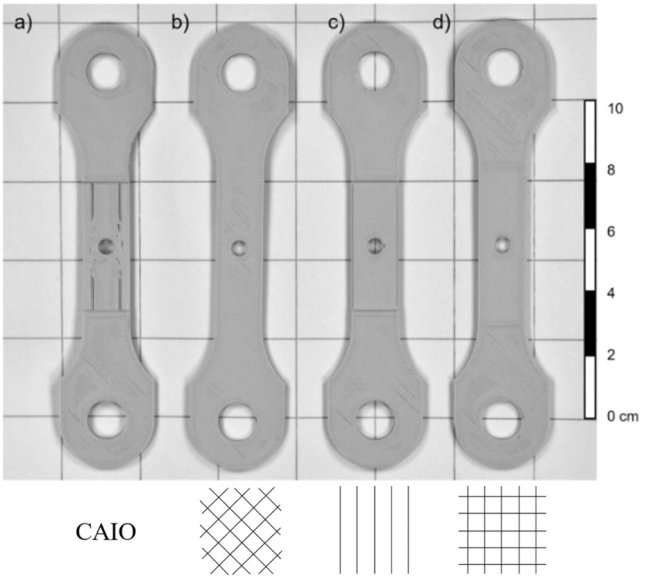

Fig. 7. Printed samples to compare CAIO optimization to standard infill patterns: a) CAIO optimized; b) + /- 45° line pattern; c) longitudinal lines (0°); d) alternating longitudinal and transverse (0°/90°) line pattern.

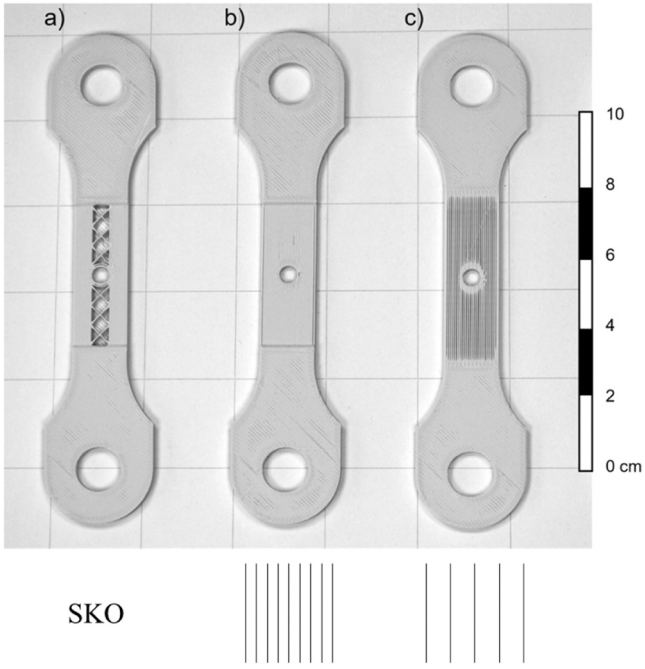

Fig. 8. Printed samples to compare SKO optimization to standard infill patterns: a) SKO optimized sample with overall 75 % infill density; b) 100 % filled longitudinal line patterned and c) 75 % filled longitudinal line patterned reference sample.

without advanced reinforcement strategies. This demonstrates that the material is utilized more effectively, enabling both an increase in strength and weight saving without requiring advanced materials or complex manufacturing steps.

The load case under consideration in this study, stresses the rim areas of the SKO optimized specimens with tension. The printing paths therefore there are along the direction of loading. Due to the adapted structure, the stress distribution in the SKO samples is more homogeneous than in the reference ones. With that the notch effect around the hole is reduced. Despite a reduced mass, this leads to an increase in tensile strength of 5 % compared to the completely filled specimen. The results show that the notch effect is more critical to failure than the reduction of material. It is noteworthy that the SKO optimized specimens broke at the transition zone from the clamping to the tested area and not at the hole. This underlines the reduction of the notch effect of the hole by optimization, even to a degree that the notch effect at the transition zone became critical to failure.

Using the CAIO and SKO approaches, the optimization is independent of the specific material used in the FFF process. Therefore, similar strengthening effects can be expected when applying the same optimization methods to other printable materials. PLA was chosen for this study due to its widespread use in 3D printing. While the absolute breaking loads will differ with alternative materials, the qualitative trends, particularly those related to anisotropy induced by the manufacturing process, are expected to remain comparable.

A key limitation of the current approach lies in the manual extraction

Table 3
Average weighted and calculated mass of all tested specimen types.

Type	Weighted mass and standard deviation [g]	Theoretically calculated mass [g]	Theoretically mass without reinforcement layer [g]
CAIO	10.903 (0.037)	10.899	9.032
	8.980 (0.018)	9.021	9.021
	10.881 (0.021)	10.831	8.989
	9.006 (0.017)	8.984	8.984

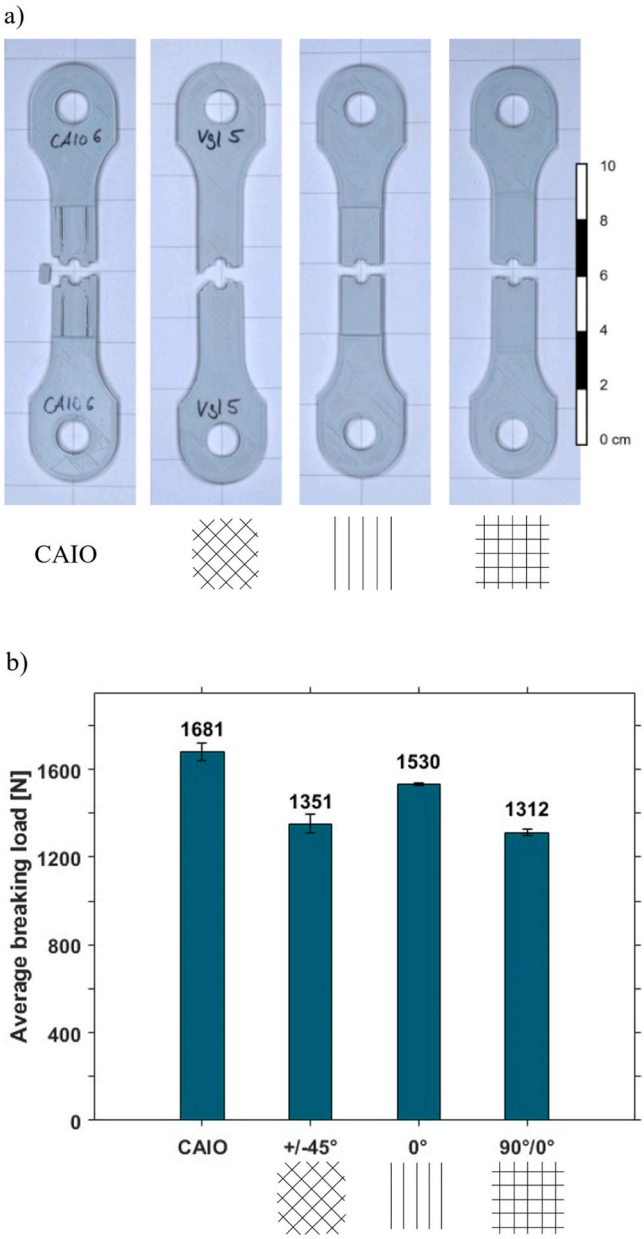

Fig. 9. a) Samples after tensile testing, left to right: CAIO, + /-45°, 0° and 0°/90°, b) associated average breaking loads and standard deviations. CAIO optimization increased the average breaking load by 10–28 %.

of the print trajectories from the ANSYS FEM results, which would be tedious for complex geometries. To enable scalable application of CAIO and SKO, the development of a more automated and integrated workflow is essential.

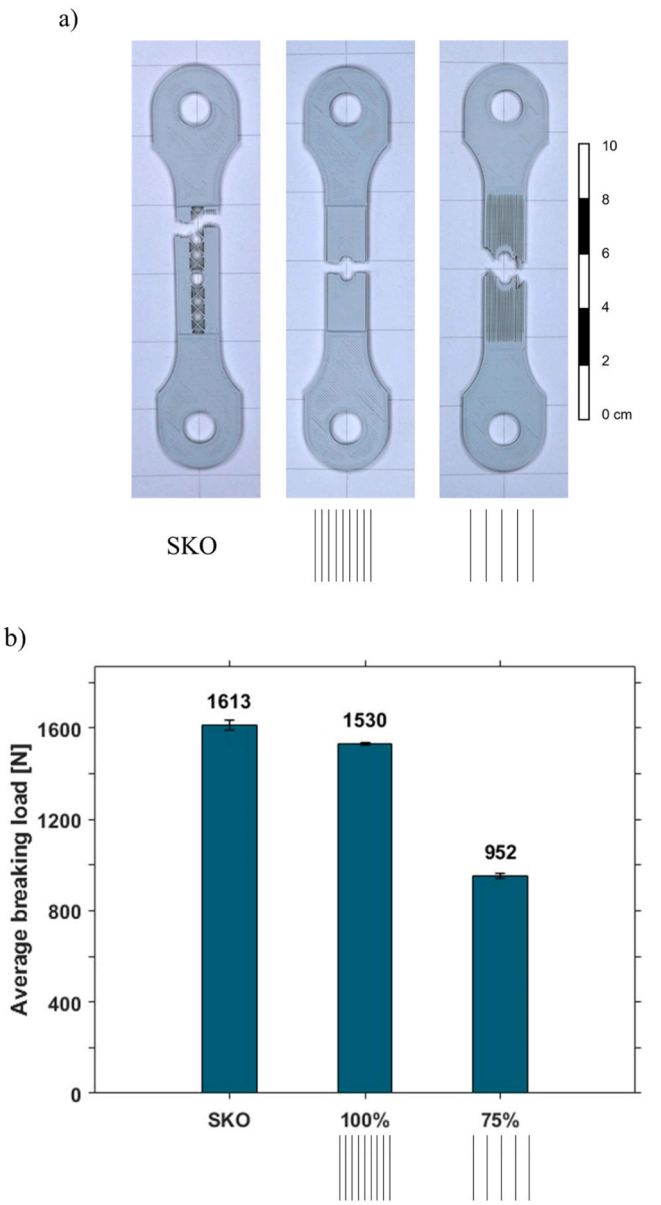

Fig. 10. a) Samples after tensile testing. Left to right: SKO, reference samples with 100 % and 75 % infill density, b) average breaking loads and standard deviations. SKO optimization increased the average braking load by 5 % despite a 25 % reduction in used material.

This study focused on a simple and symmetrical sample geometry under a uniaxial loading condition. Transferring the approaches of this work to more complex geometries with multi axial loading state is feasible with our in-layer optimization. Moreover, optimization strategies in the third dimension remain an open area for exploration, with potential in extending to techniques such as Computer Aided Optimization (CAO) to adapt not only internal structures but also the external geometry of parts [20]. While this study focused on tensile strength, future work will expand to include dynamic and more complex loading conditions and sample geometries, in order to deepen the understanding of the mechanical behavior of optimized 3D printed components.

5. Conclusions

In this study biomechanically derived optimization methods were

applied to Fused Filament Fabrication of notched tensile specimens printed in PLA. Our results demonstrate the successful transfer of these optimization techniques, called CAIO and SKO, to FFF 3D printing. Such optimizations offer powerful tools for tailoring the internal structure of components according to their specific loading conditions. The CAIO method, used with ANSYS MAPDL, aligns the highest stiffness, defined in the orthotropic material property axis, with the local principal stress direction in an iterative process, which was shown to converge extremely fast. Based on this, the printing paths were oriented along the resulting principal stress trajectories, ensuring that the printed strands are loaded along their highest loadbearing capacity. By concentrating the CAIO optimization on regions that are identified as critical to failure prior to optimization, our approach efficiently enhances component strength. The SKO optimization, in contrast, modifies the stress distribution by increasing stiffness in highly loaded areas, while simultaneously reducing it in less loaded regions. In our approach, this stiffness distribution is mapped to the printed part via different infill densities. By reducing the infill density in low loaded areas, an overall material reduction was achieved. Highly loaded regions were printed with a line pattern aligned to the loading direction, thereby optimizing the inner structure while enabling lightweight design. Overall, the following conclusions can be drawn:

- Printing along principal stress trajectories following CAIO optimization, inspired by to tree-growth mechanics, improves tensile strength by at least 10 % and up to 28 %, compared to industry standard patterns using the same amount of printed material.
- Focusing the optimization efforts on highly stressed regions allows for an effective improvement of mechanical performance while limiting the complexity and effort of the optimization.
- Adapting the infill density based on load cases using SKO, a method inspired by bone mineralization, and tailoring the remaining infill can significantly reduce notch effects introduced by sample geometry.
- Reducing the infill density in low-stressed regions by 80 % results in a 25 % decrease in overall sample mass, without compromising performance.
- Despite a 25 % reduction in material usage, a 5 % increase in tensile strength compared to industry standard prints is possible.

CRediT authorship contribution statement

Amelie Schiele: Writing – original draft, Formal analysis, Data curation. **Iwiza Tesari:** Writing – review & editing, Visualization, Supervision, Methodology, Conceptualization. **Christian Greiner:** Writing – review & editing, Supervision, Resources, Project administration, Funding acquisition, Conceptualization.

Declaration of Competing Interest

The authors declare that they have no known competing financial interests or personal relationships that could have appeared to influence the work reported in this paper.

Acknowledgements

Funding of this work has been provided by the Carl Zeiss Stiftung within CZS Center KRAFt.

Data availability

Code for generating printing paths based on CAIO is available under the link https://publikationen.bibliothek.kit.edu/1000185212, DOI 10.35097/nwybaufe27fuzw07

References

[1] J. Steuben, D.L. Van Bossuyt, and C. Turner, "Design for Fused Filament Fabrication Additive Manufacturing," presented at the ASME 2015 International Design Engineering Technical Conferences and Computers and Information in Engineering Conference, American Society of Mechanical Engineers Digital Collection, Jan. 2016. doi: 10.1115/DETC2015-46355.
[2] H. Völkl, J. Mayer, S. Wartzack, Strukturmechanische Simulation additiv im FFF-Verfahren gefertigter Bauteile, in: R. Lachmayer, K. Rettschlag, S. Kaierle (Eds.), Konstruktion für die Additive Fertigung 2019, Springer, Berlin, Heidelberg, 2020, pp. 143–157, https://doi.org/10.1007/978-3-662-61149-4_10.
[3] A. Tzotzis, A. Manavis, N. Efkolidis, C. García-Hernández, P. Kyratsis, Analysis of the Influence of Structural Characteristics on the Tensile Properties of Fused Filament Fabricated ABS Polymer Using Central Composite Design, Appl. Mech. 5 (Dec. 2023) 20–35, https://doi.org/10.3390/applmech5010002.
[4] J. Bonada, M.M. Pastor, I. Buj-Corral, Influence of Infill Pattern on the Elastic Mechanical Properties of Fused Filament Fabrication (FFF) Parts through Experimental Tests and Numerical Analyses, Art. no. 18, Materials 14 (18) (Jan. 2021), https://doi.org/10.3390/ma14185459.
[5] E. Cuan-Urquizo, E. Barocio, V. Tejada-Ortigoza, R.B. Pipes, C.A. Rodriguez, A. Roman-Flores, Characterization of the Mechanical Properties of FFF Structures and Materials: A Review on the Experimental, Computational and Theoretical Approaches, Art. no. 6, Materials 12 (6) (Jan. 2019), https://doi.org/10.3390/ma12060895.
[6] C. Casavola, A. Cazzato, V. Moramarco, C. Pappalettere, Orthotropic mechanical properties of fused deposition modelling parts described by classical laminate theory, Mater. Des. 90 (Jan. 2016) 453–458, https://doi.org/10.1016/j.matdes.2015.11.009.
[7] R. Bartosiak, F. Kaźmierczyk, P. Czapski, The Influence of Filament Orientation on Tensile Stiffness in 3D Printed Structures—Numerical and Experimental Studies, Materials 16 (15) (July 2023) 5391, https://doi.org/10.3390/ma16155391.
[8] H. Gonabadi, A. Yadav, S.J. Bull, The effect of processing parameters on the mechanical characteristics of PLA produced by a 3D FFF printer, Int. J. Adv. Manuf. Technol. 111 (3) (Nov. 2020) 695–709, https://doi.org/10.1007/s00170-020-06138-4.
[9] J. Brinkmann, T. Kaufmann, C. Martin, M. Neises, A. Schmidt, H. te Heesen, Untersuchung der Zugfestigkeit von FLM-Zugproben aus PLA bei Variation von Schichtdicke und Füllgrad, RTejournal 2016 (Oct. 2016).
[10] E. Penner, I. Caylak, R. Mahnken, Experimental Investigations of Carbon Fiber Reinforced Polymer Composites and Their Constituents to Determine Their Elastic Material Properties and Complementary Inhomogeneous Experiments with Local Strain Considerations, Fibers Polym. 24 (1) (Jan. 2023) 157–178, https://doi.org/10.1007/s12221-023-00122-x.
[11] V.S. Jatti, et al., Optimization of tensile strength in 3D printed PLA parts via meta-heuristic approaches: a comparative study, Front. Mater. 10 (Jan. 2024), https://doi.org/10.3389/fmats.2023.1336837.
[12] R. Lachmayer, K. Rettschlag, S. Kaierle, Konstruktion für die Additive Fertigung 2019, 1. Aufl. 2020, Springer Berlin Heidelberg, Berlin, Heidelberg, 2020, https://doi.org/10.1007/978-3-662-61149-4.
[13] M.K. Thompson, et al., Design for Additive Manufacturing: Trends, opportunities, considerations, and constraints, CIRP Ann. 65 (2) (Jan. 2016) 737–760, https://doi.org/10.1016/j.cirp.2016.05.004.
[14] H. Voelkl, M. Franz, D. Klein, S. Wartzack, Computer Aided Internal Optimisation (CAIO) method for fibre trajectory optimisation: A deep dive to enhance applicability, Des. Sci. 6 (Jan. 2020) e4, https://doi.org/10.1017/dsj.2020.1.
[15] B. Bhushan, Biomimetics: Bioinspired Hierarchical-Structured Surfaces for Green Science and Technology, vol. 279, in: Springer Series in Materials Science, 279, Springer International Publishing, Cham, 2018, https://doi.org/10.1007/978-3-319-71676-3.
[16] D. Kretschmann, "Mechanical properties of wood," *Wood Handb. Wood Eng. Mater. Chapter 5 Centen.* Ed Gen. Tech. Rep. FPL GTR-190 Madison WI US Dept Agric. For. Serv. For. Prod. Lab. *2010 P 51-546*, vol. 190, p. 5.1-5.46, 2010.
[17] C. Mattheck, Design in Nature, Springer, Berlin, Heidelberg, 1998, https://doi.org/10.1007/978-3-642-58747-4.
[18] P. Liu, et al., Effects of Mechanical Stress Stimulation on Function and Expression Mechanism of Osteoblasts, Front. Bioeng. Biotechnol. 10 (Feb. 2022), https://doi.org/10.3389/fbioe.2022.830722.
[19] S.C. Cowin, Mechanical modeling of the stress adaptation process in bone, Calcif. Tissue Int. 36 (1) (1984) S98–S103, https://doi.org/10.1007/BF02406141.
[20] C. Mattheck, K. Bethge, The Structural Optimization of Trees, Naturwissenschaften 85 (1) (Jan. 1998) 1–10, https://doi.org/10.1007/s001140050443.
[21] D. Reuschel, C. Mattheck, Optimization of fiber arrangement with CAIO (Computer aided internal optimization) and application to tensile samples, WIT Trans. Built Environ. 40 (1999) 1–9, https://doi.org/10.2495/OP990231.
[22] J.D. Reuschel, Untersuchung der Faseranordnung natürlicher Faserverbunde und Übertragung der Ergebnisse auf technische Bauteile mit Hilfe der Finite-Elemente-Methode, Dissertation (1999), https://doi.org/10.5445/IR/11799.
[23] *DIN EN ISO 527–1:2019–12, Kunststoffe_- Bestimmung der Zugeigenschaften_- Teil_1: Allgemeine Grundsätze (ISO_527–1:2019); Deutsche Fassung EN_ISO_527–1:2019*. doi: 10.31030/3059426.
[24] A. Öchsner, R. Makvandi, Plane Finite Elements for Two-Dimensional Problems: Application of the Computer Algebra System Maxima, Springer International Publishing, Cham, 2021, https://doi.org/10.1007/978-3-030-89550-1.
[25] A. Baumgartner, L. Harzheim, C. Mattheck, SKO (soft kill option): the biological way to find an optimum structure topology, Int. J. Fatigue 14 (6) (Nov. 1992) 387–393, https://doi.org/10.1016/0142-1123(92)90226-3.

[26] N.H. Hart, S. Nimphius, T. Rantalainen, A. Ireland, A. Siafarikas, R.U. Newton, Mechanical basis of bone strength: influence of bone material, bone structure and muscle action, J. Musculoskelet. Neuron Inter. 17 (3) (Sept. 2017) 114–139.
[27] L. Harzheim, G. Graf, Optimization of Engineering Components with the SKO Method, SAE Trans. 104 (1995) 1974–1982.
[28] S. Matsos, "Getting Started with G-code | 3D Bioprinting," Allevi. Accessed: Nov. 26, 2024. [Online]. Available: ⟨https://www.allevi3d.com/guide-to-gcode/⟩.
[29] J. Merkert, "Bewegungsprogramm: G-Code verstehen, programmieren und mit Python generieren," *c't*, vol. 2017, no. 25, Heise, p. 174, Nov. 24, 2017.
[30] P. Bengfort, "Entwicklung einer Prozessmodifikation für teilkristalline Thermoplaste im Fused Layer Modeling," 2023, Accessed: Nov. 22, 2024. [Online]. Available: ⟨http://hdl.handle.net/2003/42281⟩.
[31] Md. Qamar Tanveer, G. Mishra, S. Mishra, R. Sharma, Effect of infill pattern and infill density on mechanical behaviour of FDM 3D printed Parts- a current review, Mater. Today Proc. 62 (Jan. 2022) 100–108, https://doi.org/10.1016/j.matpr.2022.02.310.
[32] A. Yadav, et al., Fused filament fabrication: A state-of-the-art review of the technology, materials, properties and defects, Int. J. Interact. Des. Manuf. IJIDeM 17 (6) (Dec. 2023) 2867–2889, https://doi.org/10.1007/s12008-022-01026-5.
[33] V. Krishnanand, V. Singh, A.K. Mittal, K. Branwal, Sharma, M. Taufik, Extrusion strategies in fused deposition additive manufacturing: A review, Proc. Inst. Mech. Eng. Part E J. Process Mech. Eng. 238 (2) (Apr. 2024) 988–1012, https://doi.org/10.1177/09544089221150709.
[34] H. Völkl, Ein simulationsbasierter Ansatz zur Auslegung additiv gefertigter FLM-Faserverbundstrukturen, FAU Stud. Aus Dem Masch. 393 (2022), https://doi.org/10.25593/978-3-96147-%20524-7.
[35] V. Murugan, G. Alaimo, S. Marconi, P.Z. Berke, T.J. Massart, F. Auricchio, Filament path optimization of Fused Filament Fabricated parts incorporating the effect of pre-fusion densities, Int. J. Solids Struct. 254–255 (2022) 111916, https://doi.org/10.1016/j.ijsolstr.2022.111916.
[36] K.-M.M. Tam, C.T. Mueller, Additive Manufacturing Along Principal Stress Lines, 3D Print. Addit. Manuf. 4 (2) (June 2017) 63–81, https://doi.org/10.1089/3dp.2017.0001.
[37] G. Yan, J. Xu, T. Xiao, G. Zhang, X. Jiang, Y. Sun, Principal stress direction-aware streamlined printing path planning for fused filament fabrication, Compos. Part Appl. Sci. Manuf. 190 (Mar. 2025) 108642, https://doi.org/10.1016/j.compositesa.2024.108642.
[38] J. Butt, R. Bhaskar, V. Mohaghegh, Investigating the Influence of Material Extrusion Rates and Line Widths on FFF-Printed Graphene-Enhanced PLA, Art. no. 3, J. Manuf. Mater. Process 6 (3) (June 2022), https://doi.org/10.3390/jmmp6030057.
[39] S. Pervaiz, T.A. Qureshi, G. Kashwani, S. Kannan, "3D Printing of Fiber-Reinforced Plastic Composites Using Fused Deposition Modeling: A Status Review, Art. no. 16, Materials 14 (16) (Jan. 2021), https://doi.org/10.3390/ma14164520.

Glossary

CAIO: Computer Aided Internal Optimization
CAO: Computer Aided Optimization
FDM: Fused Deposition Modeling
FEM: Finite Element Method
FFF: Fused Filament Fabrication
PLA: Polylactic Acid
SKO: Soft Kill Option